Enhanced Schlieren System for In Situ Observation of Dynamic Light–Resin Interactions in Projection-Based Stereolithography Process

Aditya Chivate
Department of Industrial and Systems Engineering,
University at Buffalo,
The State University of New York,
401 Bell Hall, UB N Campus,
Buffalo, NY 14260
e-mail: adityatu@buffalo.edu

Chi Zhou[1]
Department of Industrial and Systems Engineering,
University at Buffalo,
The State University of New York,
401 Bell Hall, UB N Campus,
Buffalo, NY 14260
e-mail: chizhou@buffalo.edu

Digital maskless lithography is gaining popularity due to its unique ability to quickly fabricate high-resolution parts without the use of physical masks. By implementing controlled grayscaling and exposure control, it has the potential to replace conventional lithography altogether. However, despite the existence of a theoretical foundation for photopolymerization, observing the voxel growth process in situ is a significant challenge. This difficulty can be attributed to several factors, including the microscopic size of the parts, the low refractive index difference between cured and uncured resin, and the rapid rate of photopolymerization once it crosses a certain threshold. As such, there is a pressing need for a system that can address these issues. To tackle these challenges, the paper proposes a modified Schlieren-based observation system that utilizes confocal magnifying optics to create a virtual screen at the camera's focal plane. This system allows for the visualization of the minute changes in refractive indices made visible by the use of Schlieren optics, specifically the deflection of light by the changing density-induced refractive index gradient. The use of focusing optics provides the system with the flexibility needed to position the virtual screen and implement optical magnification. The researchers employed single-shot binary images with different pixel numbers to fabricate voxels and examine the various factors affecting voxel shape, including chemical composition and energy input. The observed results were then compared against simulations based on Beer–Lambert's law, photopolymerization curve, and Gaussian beam propagation theory. The physical experimental results validated the effectiveness of the proposed observation system. The paper also briefly discusses the application of this system in fabricating microlenses and its advantages over theoretical model-based profile predictions. [DOI: 10.1115/1.4062218]

Keywords: Schlieren optics, projection stereolithography, additive manufacturing, refractive index gradient, rapid prototyping and solid freeform fabrication

1 Introduction

Additive manufacturing (AM) is a disruptive technology that has paved the way for numerous applications ranging from sub-micron part fabrication to large-scale product manufacturing. It has been gaining popularity over the years owing to its distinctive ability to produce intricate structures with high resolution, customizability, and speed. Projection-based stereolithography (PSL) is one such technique that utilizes light projection to polymerize materials layer by layer [1]. It leverages the versatility of polymer chemistry and digital light patterning to produce complex parts with programmable optical, electrical, mechanical, and biomedical properties [2–4]. Compared to other AM processes, PSL has significant advantages, particularly in high resolution and accuracy. The printing resolution is governed by the light intensity, exposure time, material properties, and light–material interaction [5]. Despite these advantages and the growing enthusiasm, implementation in a manufacturing environment, especially on the sub-millimeter scale, has lagged. Some of the common problems include the limited understanding of the fundamentals of polymerization, the effect of additives, and energy-time dynamics.

The PSL process is a photopolymerization process where liquid photopolymers containing monomers and oligomers can be manipulated to achieve specified physical properties following a multistage dynamic process. In order to improve the printing resolution, it is essential to understand the light–material interaction for each layer and how parts grow through layers. Scientists have long relied on the theoretical understanding of how photopolymerization works and have developed empirical relations of the curing process. The preliminary investigation on understanding the photopolymerization process was detailed in the early 60 s [6]. The chemistry-based models discussed in the research described how the initiation and propagation phase progresses. Though this was essential research considering its significance in acrylate-based coatings, it was not until 1974 that photopolymerization was used for AM [7]. Due to the complex chemical reaction process, the research on the polymerization process for PSL is still limited to the bulk polymerization models to understand the underlying mechanism and optimize the printing process. Conventional models designed for a large number of pixels fail to understand how a single-pixel or a small number of pixels grow, which plays a vital role in controlling the process resolution and accuracy. Furthermore, while these models were based on experimental data collected over the years, observing them in real-time is still challenging. The models are based on ideal conditions, but numerous other factors affect the process in practice. Despite the long history of vat

[1]Corresponding author.

Manuscript received January 27, 2023; final manuscript received March 18, 2023; published online April 12, 2023. Assoc. Editor: Robert Chang.

photopolymerization techniques, an understanding of how the polymerization process takes place is still lacking.

The *in situ* experimental verification is challenging due to the low refractive index of the polymerized part. It is challenging to observe the part with the naked eye as well as cameras due to the low refractive index difference between the cured part and the resin. Semi-cured gel-like resin is more difficult to observe, and distinguishing the cured, semi-cured, and uncured components is very challenging if not impossible with current approaches. An observation system with adjustable focal length and relatively shorter depth of focus is required to observe this tiny part (cured by a single or a small number of pixels) growth. Observation systems with a shallow depth of focus often require them to be placed very close to the object, which is challenging as the part is inside the vat during the printing process. The polymerization process is dynamic, nonlinear, and extremely rapid once the energy threshold is crossed. It is highly desirable to develop a high-efficiency, high-fidelity system to observe the nonlinear and dynamic process in real-time to understand the photopolymerization mechanism and accordingly calibrate and optimize the PSL system to achieve improved resolution and efficiency.

Digital cameras can observe parts that are fairly large and surrounded by media with a lower refractive index [8]. Most current approaches cure the resin with different exposure dosages and then clean the parts for observation [9]. This approach is tedious and error-prone, and more importantly, it cannot capture the semi-curing process, which is an important factor in defining the surface finishing of the printed part. The refractive index changes can provide an implication about the amount of polymerization. The *in situ* refractive index measurement setups are quite complex and need to be inserted in the vat [10]. Total internal reflection (TIR)-based refractive index measurement is popular, but it uses a laser-based system that is difficult to set up. It is also limited by the fact that it can measure the refractive index of the complete region under consideration rather than focusing on a small region of interest [7]. Some in situ measurements rely on the functional groups present in the media under consideration. It uses the optical properties of the media; i.e., it absorbs a particular wavelength and disperses others. In the PSL process, as there is no significant change in the functional groups, this technique is not suitable [11]. Individual pixel size is too small to be seen by the naked eye. Current observation systems lack the sophistication to observe such small parts inside a multi-material system. Micron-scale features require highly focused images. Observation systems using a beam splitter and a complementary metal-oxide semiconductor (CMOS) camera were designed to observe the focal plane. Though such a system was capable of achieving focused images, it cannot capture the voxel growth [12,13].

We hypothesize that a system with low refractive index contrast, high magnification, and adjustable focus can address these challenges. We propose a modified schlieren optical system based on shadowgraph. Shadowgraph is an optical method that can uncover irregularities in transparent media by utilizing the bending of light due to a change in refractive index [14]. This gradient of the refractive index is directly related to the gradient of flow density. This technique is relatively simple in terms of required equipment, as it just requires light and a screen to capture images. In principle, the system just requires light and a screen to record the images. A shadow is generated as the light ray is refractively deflected, so the position on the plane where the undeflected light ray would arrive now remains dark. At the same time, the region where deflected light arrives now appears brighter, and a visible pattern of contrast is now produced on the imaging plane. As it is just governed by light, by adjusting the distance between the object and the imaging plane, we can account for a wide range of refractive index changes. Schlieren optics have long been used to observe fluid flows with varying densities, which allows us to observe semi-cured resin.

A simple shadowgraph can provide us with the ability to observe high-contrast images but fails to address the challenge of imaging small parts. We propose a two-level magnification system to address this issue. Higher magnification requires a shallower depth of view. The magnification for observing a part that is a few microns in width comes with a focusing depth of a few millimeters. For vat polymerization, it is not possible to achieve this with conventional approaches due to the system's inaccessibility. To address this issue, we propose a system that uses a virtual plane to focus the image, which is later magnified to the required degree using confocal optics. The confocal optics result in greater resolution, ability to control depth of focus, and reduction of background information away from the focal plane. Our system focuses on capturing high-density information in the small observation window to balance the capturing speed and resolution.

The proposed system in this paper has a high potential to capture real-time high-contrast images during the PSL photopolymerization process. It will provide significant insights into the process understanding and allow for real-time characterization and closed-loop control of the part growth. It will prove to be a vital tool for calibration and present a systematic approach to identifying curing parameters like exposure energy, curing time, the effect of dye concentration, and the effect of pixel interactions. The calibrated parameters and formulated models can be incorporated to facilitate process optimization and mask image planning. It will also provide a physical verification tool to validate the photopolymerization theories that have been adopted in the community for decades.

The remainder of the paper is organized as follows: Sec. 2 discusses the theoretical foundations and simulations for photopolymerization. Equations governing light beam propagation and photopolymerization have been detailed. Section 3 introduces the experimental setup and presents a novel design for a schlieren-based optical system for voxel observation. In Sec. 4, the simulations and robustness of the observation system are validated against the voxel growth experiments, followed by a discussion of insightful results. Finally, Sec. 5 summarizes the achievements and briefly discusses potential opportunities for future work.

2 Theoretical Foundations

PSL is one type of vat polymerization-based stereolithography process that uses ultraviolet (UV) light in the form of patterned images to selectively cure a photosensitive polymer in a layer-by-layer fashion. Traditional stereolithography uses a galvo-mirror to scan a UV laser beam across the surface of a resin vat to initiate polymerization. However, the laser-based process is limited by the size of the laser spot and requires serial scanning, which results in a slower printing speed. PSL, on the other hand, uses a spatial light modulator, such as a digital micromirror device (DMD) or liquid crystal device (LCD) to project a light pattern over the entire printing area, therefore is significantly faster owing to the parallel process [15]. As the patterned image is projected onto the resin surface, the light defined by the image cures the resin once sufficient energy is absorbed by the materials. Such a photopolymerization process is related to a variety of parameters, including light wavelength, light intensity, exposure time, and light–resin interaction.

2.1 Light Irradiance and Light–Resin Interactions.

In the PSL process, the lateral resolution is primarily controlled by the input light irradiance, including the light pattern, intensity, and time. Due to the diffraction inefficiency and dark-field diffusion caused by the projection device, the light beam of each pixel spreads to its neighboring pixels, the pixels in the image are *Gaussian* distributed rather than uniformly distributed, and the light beam will spread to its neighboring pixels such that the received light energy at each location in the working area is contributed by multiple pixels [16–18]. The light intensity at each location (x, y) of the material's top surface can be calculated by Eq. (1)

$$I(x, y, 0) = \sum_{(x_i, y_j)\in\mathcal{S}} I_{i,j}\exp\left\{-\left[\left(\frac{x-x_i}{\sigma_x}\right)^2 + \left(\frac{y-y_j}{\sigma_y}\right)^2\right]\right\} \quad (1)$$

where $(x_i,\ y_j) \in \mathcal{S}$ are the locations of the pixels which can cover (x, y), $I_{i,j}$ is the light intensity at the center of the pixel (x_i, y_j), σ_x and σ_y are parameters for the *Gaussian* profile.

The vertical resolution is related to the curing depth and is primarily controlled by the optical properties of the light traveling through the material and the chemical properties of the material. The curing depth largely depends on the reaction kinetics of the photo-initiator and polymer and is governed by Beer–Lambert's law [19]

$$C_d = D_p \ln\left(\frac{E}{E_c}\right), \quad D_p = \frac{1}{\alpha}, \quad \alpha = \alpha_{initiator} + \alpha_{absorber} \tag{2}$$

where C_d is the curing depth, D_p is the penetration depth related to the light absorption coefficient α of the material, E_c is the critical exposure energy, and E is the exposure on the resin surface, which is the product of the light intensity and exposure time.

Based on Eq. (1) and the reversed form of Eq. (2), the light intensity at each 3D location (x, y, z) of the material can be written as

$$I(x, y, z) = I(x, y, 0) \exp\left\{-\frac{z}{D_p}\right\} \tag{3}$$

The total exposure energy during the time period t is shown in Eq. (4), which defines the exposure energy received in the 4D space (x, y, z, t) of the material

$$E(x, y, z, t) = I(x, y, z)t \tag{4}$$

The surface where the energy is equal to the critical exposure energy E_c is naturally the predicted profile of the to-be-fabricated structure, which can be expressed in the following implicit formula:

$$E(x, y, z, t) = E_c \Rightarrow z = f(x, y) \tag{5}$$

By integrating Eqs. (1)–(5), an energy-based mathematic model can be formulated to establish the relationship between the geometry (shape and size) of the cured feature and the input parameters (pixel grayscale values, exposure time, and photo-absorber dose). In particular, a single pixel with a *Gaussian* profile generates a paraboloid shape, as shown in Eq. (6), which can be trivially derived from Eqs. (1)–(5)

$$x^2 + y^2 + z = D_p \ln\left(\frac{I_{\max}}{E_c}\right) \tag{6}$$

2.2 Photopolymerization Simulation. Based on the aforementioned theories, a PSL photopolymerization simulation tool was developed to study the relationship between the cured profile and the input process and material parameters. Figure 1(*a*) shows the ideal top-hat profile of a single pixel, where the top part along the energy axis represents the exposed energy on the top surface of the resin, and the bottom part along the depth axis represents the cured profile under the received energy dose and the critical energy E_c. In contrast, Fig. 1(*b*) shows the *Gaussian* profile of the actual pixel and the curing profile in the paraboloid shape. Figure 1(*c*) shows the pixel blending effect of multiple overlapped pixels [5]. The top curve along the energy axis represents the accumulative energy (Eq. (1)), and the bottom curve along the depth presents the curing profile with a top-hatted paraboloid shape.

Figures 1(*d*)–1(*e*) explain the simulated relation between the curing profile and the input parameters. Along the vertical direction, the irradiance decays from the maximum energy at the resin surface into the resin following an exponential function defined in Eq. (3) and shown by the red curve in Fig. 1(*e*). Ideally, the locations in the resin where the energy equals the critical energy E_c defines the curing profile as shown in Fig. 1(*d*). However, in reality, voxels contain photopolymers that are fluxing between stages of the photopolymerization process: going from liquid to their gel point and then on toward their full cross-linking density. A portion of the energy input is used to neutralize oxygen-free radicals, which starts short-chain polymerization that eventually leads

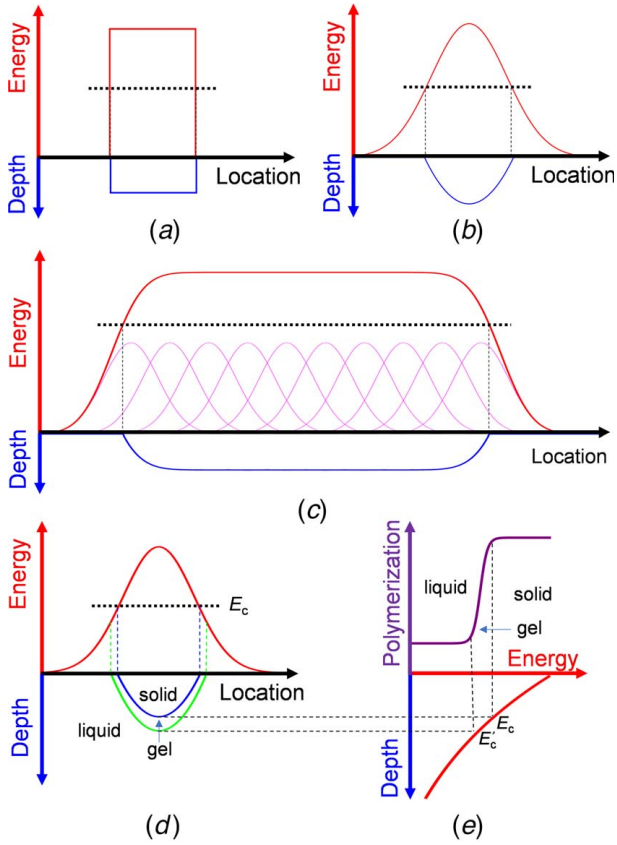

Fig. 1 PSL Photopolymerization simulation

to long-chain polymerization. The short chains produced form a semi-solid gel that plays a crucial role as a transitional phase between liquid and solid states. The critical threshold at which this gel phase occurs is represented by E_c' in Fig. 1(*e*) and dependent on the particular material being used. In practice, the gel region is more complicated than just a threshold point; the amount of gelation governs the part quality [20]. The top curve along the polymerization axis in Fig. 1(*e*) represents the real polymerization working curve, and the region between the two curves along the depth axis in Fig. 1(*d*) represents the partially cured gel structures.

2.3 Voxel Growth Simulation. Three-dimensional voxel growth simulations were developed based on Eqs. (2), (3), and (6). The simulation takes into consideration the light spreading at each individual illuminated pixel and the additive effect of multiple neighboring pixels. The simulation allows for adjustability of the curing depth and the light spreading which can be tuned to adjust the material properties and the illumination wavelength.

3 Experimental Setup and System Design

The experimental setup consisted of two main components, a projection-based photocuring setup, and a schlieren-based observation setup.

3.1 Digital Light Projection System. In this research, a mercury lamp combined with a 365-nm UV filter is used for illumination. A 0.37 NA light guide with a 3-mm output diameter was used to deliver light. With the UV filter and at 80% of the light output, the measured irradiance was 35 mW/cm^2, respectively. An achromatic doublet lens with $f = 200$ mm was used to collimate the light beam to a spot size enough to cover the DMD. A high-performance light engine from Vialux was used for pattern

generation. The DMD has a resolution of 1920 × 1080 with an individual micromirror measuring 10.8 μm on each side and a pitch of 1 μm. The light reflecting from the DMD was passed through a set of focusing lenses to form a focused image on the vat surface. A mirror was used to direct light vertically, making the setup compact. Changing the optics allows us to change the size of the projected image. The advantage of this setup lies in the customizability. The light engine was combined with adjustable optics, which enabled adjustable magnification for enlarging the projected image. The optical system was tuned to achieve 1.5:1 magnification. A bi-telecentric configuration was used for the projection system. A telecentric system ensures constant magnification regardless of the object's distance or location in the field of view. As the objective of this study was to understand the pixel growth dynamics, a stationary platform submerged in the vat was used. Binary masks were projected from the bottom of the vat made from all-side clear UV transparent cuvette. A high-speed CMOS camera from AmScope was used to capture the voxel growth process. A white LED with a light guide was used for illuminating the schlieren setup. The configuration of the observation and projection system can be seen in Fig. 1.

3.2 Schlieren Observation Setup. Schlieren system is not a brand new technique but has been in use since the seventeenth century. Robert Hooke first demonstrated this method in 1665 [21]. The conventional schlieren system, from which this work is inspired, was developed in 1859 [22] and later modified in 1864 by Töepler. It uses a point source to illuminate the test section, and the image is formed by converging lenses. The image location is the conjugate distance based on the thin lens equation: $1/f = 1/d_o + 1/d_i$ where f is the focal length of the lens, d_o is the distance between the test object and the lens, and d_i is the distance between the image and the lens. Schlieren is a technique that allows us to see the changes in the composition or densities of a transparent medium. The basis of schlieren imaging originated from Snell's law, which states that light slows down when it passes through an optically denser medium. When light encounters an inhomogeneous medium like fluids in motion, light deflects from its path, and we obtain a schlieren. Variations in the working fluid's density cause the light rays to deviate from the original paths, deflecting away from the focal point. When a knife-edge is inserted at the focal point, rays deflected in one direction from the parallel would be prevented from reaching the viewing screen. This elimination of rays from the image resulted in a variation of illumination at the screen, which is proportional to the first derivative of the density variation in the working fluid. Though the blade is just to block half the light, if it is used in perpendicular orientation to the flow axis, the density gradients will enlighten or darken based on which side of the knife-edge they are located. A color filter can also be used instead of the knife-edge to increase the contrast and visualization effect of the projected image [23–25]. A schematic of used schlieren based observation system can be seen in Fig. 2.

Rudimentary lens-based schlieren system uses a straight-line arrangement of lenses to visualize the schlieren. As shown in Fig. 3, a beam of light emanating from the point source is collimated using lens L_1. This parallel beam of light is then deflected by the test subject S and is passed through second lens L_2, where it focuses on the knife-edge K. Lenses L_2 and L_3 (a magnifying/projection lens) focus the schlieren image onto a screen or camera sensor S.

The lens arrangement is made so that the growing voxel is placed approximately at the focus of lens L_2, and the knife-edge is placed at a distance f from lens L_2 in the opposite direction. From the thin lens magnification formula, if the object is placed on $2f$, the formed image is the same size as the object. The actual size of the cured part is a few microns. In order to get a 2× magnified image on the virtual screen, we placed the second lens L_3 at $0.5f$ from the knife-edge. The image is formed at a distance f from the lens on a virtual screen which is further magnified with an objective lens attached to a confocal microscope system.

Refractive index-dependent techniques like schlieren imaging depend on the unique refractive index–density change relation described by the Lorentz–Lorenz formula

$$\frac{n^2 - 1}{\rho(n^2 + 2)} = \text{constant} \tag{7}$$

where n is the refractive index, and ρ is the density of the material. The constant is dependent on the chemical composition of the resin and does not deviate much with changing wavelength. Image formation in schlieren is caused due to light deflection in variable refractive index media with light rays bending toward the region of higher refractive index.

3.3 Principle of Schlieren Observation System. To understand the principle behind the schlieren optics, we assume a vertical refractive index gradient $\partial y/\partial x$ and no gradient in the x- and z-direction. This provides a simple deconstruction of the problem in 2D without loss of generality. A planar light wave, which is vertical initially, is displaced after passing through the schlieren. The distance covered per unit time is given by $\Delta x/\Delta t$, and the angle by which the ray is refracted is $\Delta\theta$. Refractive index is defined as

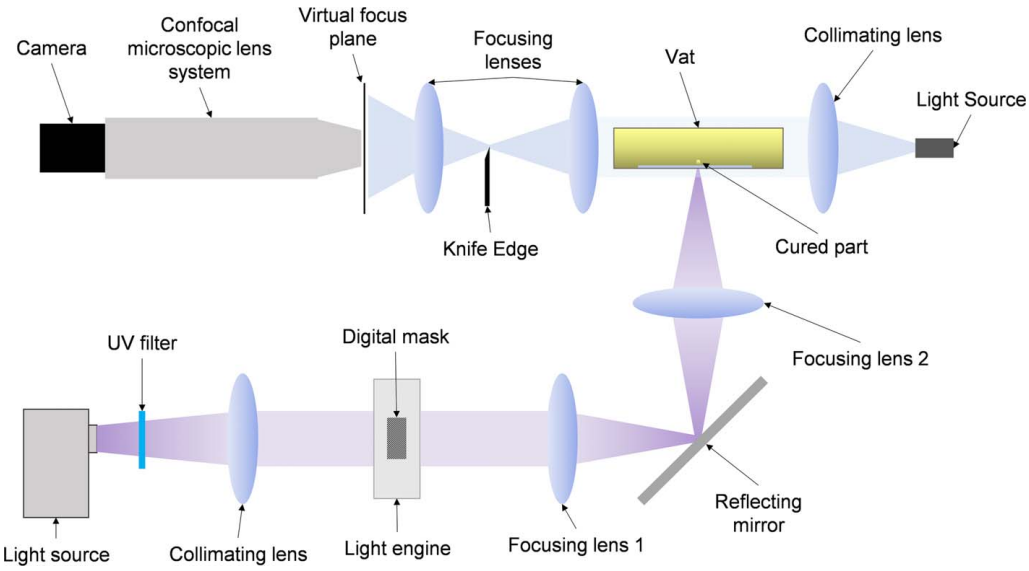

Fig. 2 Schematic of the projection and observation system

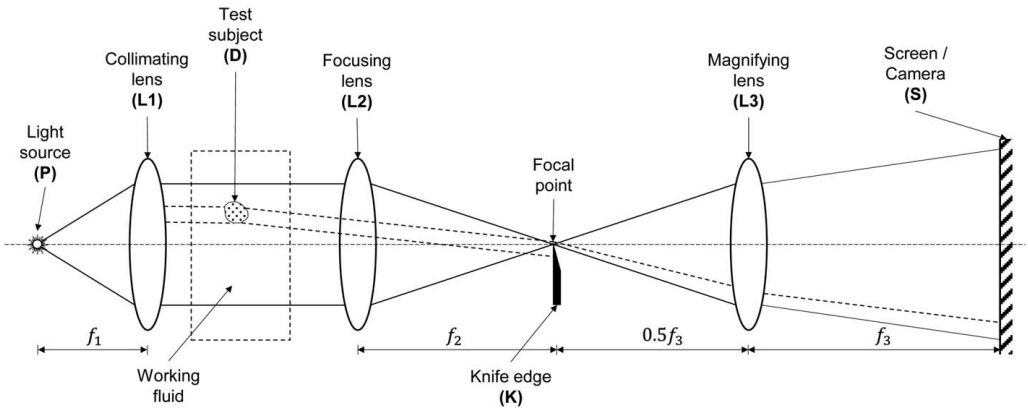

Fig. 3 Schematic showing the path of the light beam in the lens-based schlieren system

the ratio of the speed of light in the vacuum to the speed of light in the medium under consideration: $n = c/v$. From Fig. 4(*a*), using small-angle approximation

$$\Delta\theta = \frac{c/n_2 - c/n_1}{\Delta y}\Delta t \tag{8}$$

where n_1 and n_2 are the refractive indices of the two media, respectively. Differential time can be represented as $\Delta t = \Delta x \times n/c$. Therefore, the angle of refraction becomes

$$\Delta\theta = \frac{n}{n_1 n_2}\frac{n_1 - n_2}{\Delta y}\Delta x \tag{9}$$

On simplifying the terms, we obtain

$$\frac{\Delta\theta}{\Delta x} = \frac{1}{n}\frac{\Delta n}{\Delta y} \tag{10}$$

Using small-angle approximation $d\theta = dy/dx$, we get

$$\frac{d^2y}{dx^2} = \frac{1}{n}\frac{dn}{dy} \tag{11}$$

Relating the curvature of refracted light to the magnitude of the refractive index gradient indicates that the ray deflection is caused by the refractive index gradient and not the refractive index itself.

In this setup, the knife-edge is placed at the focal point of the second lens and is adjusted such that a set amount of light is cut off. Let s_0 be the original size of the focused beam and s_k be the size of the beam after it has been cut off by the knife-edge. I_0 is the illumination on the screen when no knife-edge is present and I_k is the illumination with knife-edge positioned. The illumination on the screen without any disturbance in the test section is given by

$$I_k = \frac{s_k}{s_0}I_0 \tag{12}$$

For the purpose of this paper, the s_k was set at about 50%.

When the light passes through the test region, the light beam deflects in response to the refractive index change. Let this deflection be Δs. Let the final illumination after light passes through the test region be given by I_f. From Eq. (12)

$$I_f = \frac{s_k + \Delta s}{s_k}I_k \tag{13}$$

The light intensity change is given by $\Delta I = I_f - I_k$, and the contrast as a result of this shift is represented as

$$\text{contrast} = \frac{\Delta I}{I_k} = \frac{\Delta s}{s_k} \tag{14}$$

As the angle is small, $\Delta s = \Delta\theta \times f_2$, where f_2 is the focal length of the second lens

$$\text{contrast} = \frac{\Delta I}{I_k} = \frac{f_2\Delta\theta}{s_k} \tag{15}$$

By changing the location of the knife-edge in the y-direction, the contrast can be adjusted to suit the resolution.

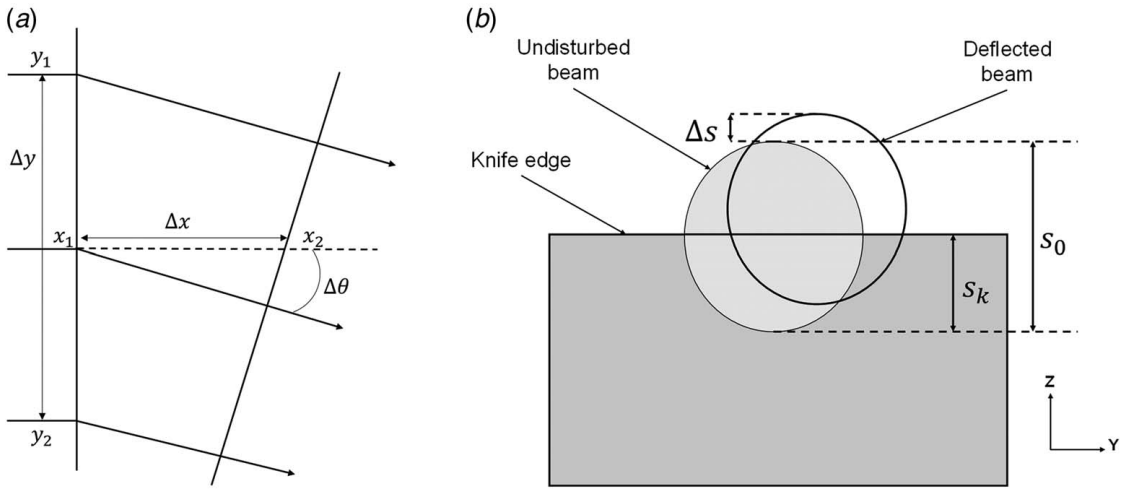

Fig. 4 (*a*) Bending of a light ray in the vertically stratified fluid medium due to refraction [24] and (*b*) schematic of the undisturbed and disturbed light beam at the knife-edge cross section [35]

3.4 Resolution and Accuracy of Schlieren. The accuracy and resolution of the lens-based schlieren system depend on various factors like the optical components, light source, and the sensitivity of the detector used for capturing the schlieren images. The lens-based schlieren system presented in this research was tested to measure the changes in the refractive index on the order of 10^{-3}.

In terms of the resolution, the spatial resolution of the schlieren system depends on the spot size, lens aperture, and the distance between the object and the lens. The diffraction-limited resolution of the schlieren system is about 600 nm. However, the actual resolution also depends on the resolution of the detector. The proposed system uses a 5MP camera (pixel size of 5.6 μm) at a resolution of 640×480 and illumination wavelength of 550 nm giving a spatial resolution of 1.1 μm.

4 Results and Discussion

In this section, we present the experimental validation using the freeform voxel growth experiments. The simulation model is validated against some experimental measurements based on the proposed Schlieren system. Particularly, the penetration depth, light intensity, and shape of the growing voxel are measured and compared against the simulated results and SEM characterizations.

4.1 Materials and Methods. An acrylate-based resin was prepared consisting of poly(ethylene glycol) diacrylate (PEGDA $M_w = 250$ and 575 g mol^{-1}) as monomer and phenylbis(2,4, 6-trimethylbenzoyl) phosphine oxide (Irgacure 819) as initiator both from Sigma Aldrich. 2-Nitrophenyl phenyl sulfide (NPS) procured from TCI Chemicals was used as a dye. Monomer–initiator ratio of 97:3 was chosen. Two samples with 0.25% and 1% dye were prepared to achieve desired penetration depth. Two sets of experiments were performed using different dye concentrations. PEGDA was preferred as it is transparent to visible light and is more responsive to 365 nm wavelength, thus reducing the possibility of photopolymerization due to the illumination used for the observation system. PEGDA has a significantly smaller refractive index change after polymerization, which instills the need for a better observation system. For materials opaque to visible light, other wavelengths can be used. The prepared PEGDA 250 resin has a refractive index of 1.463 and a density of 1.11 g/cm^3. After photopolymerization, the refractive index of the cured resin changes to 1.601. The trend in refractive index change with the degree of photopolymerization is linear.

Using the voxel growth experiments, the simulation model is validated by comparing the experimentally measurable growth profile. Circular masks with different numbers of binary pixels were used. A constant light intensity of 35 mW/cm^2 was used for all the projected patterns with different exposure times based on the number of pixels. The cured part was compared against the simulation results. The model parameters were derived from a theoretical understanding of light propagation and light–resin interactions. Such a comparison demonstrates that the proposed model accurately describes the voxel curing process. The light intensity drops to about 85% of the maximum intensity value at 500 μm from the focal plane. The penetration depth for the resin chosen for the experiments was far less than 500 μm; thus, the effect due to the evolution of the light intensity profile was not considered, and it was assumed to be the same in the vertical region of consideration [13].

4.2 Validation: Observing Low Refractive Index Material. While schlieren and shadowgraph both exploit the effects of light refraction in a non-homogenous transparent medium to generate regions of varying contrast, the quality and resolution of the images differ from technique to technique. Shadowgraph imaging is based on beam deflection and displacement, whereas schlieren imaging is based solely on beam deflection [26]. Shadowgraph imaging requires the simplest setup, but the generated image data are quite complicated. It is difficult to analyze the data, which requires solving complex Poisson equations for different boundary conditions. The images convey less details about the refractive index gradient. Schlieren, on the other hand, has modest demands on the instrumentation complexity, and the generated data are easier to process. Interferometry is another such technique that uses differences in the refractive index to form images, but the technique requires a sophisticated setup and is extremely sensitive to alignment. For these reasons, it was not considered in this research. As can be clearly seen from Fig. 5(*a*), despite the change in refractive index, it is not possible to observe the cured part using the camera alone. This is primarily caused by the low refractive index difference between the liquid and solidified resin. While shadowgraph is easier to set up, the images are difficult to process (Fig. 5(*b*)). Schlieren images, on the other hand, give images that perfectly represent the contrast caused by changes in refractive index gradient during the photopolymerization (Fig. 5(*c*)). The comparison between the different observation systems validated that the proposed schlieren system can successfully observe the cured resins surrounded by liquid pre-polymers with low refractive index difference, therefore providing a powerful tool to study the complex photopolymerization process in real-time.

4.3 Validation: Observing Small-Sized Voxel(s). A freeform voxel is cured by shining a single-shot binary UV pattern through a stationery UV transparent glass cuvette. The PSL printing approach is used in this process, where the part is created by frontal photopolymerization, which begins on the glass substrate and expands toward resin depths. The DMD allows us to shine desired grayscale/binary image patterns onto the substrate. The part height is governed by the grayscale, exposure time, and the chemical barriers caused by the penetration depth. As shown in Fig. 6, illumination of a circular binary image results in an axisymmetric convex part. As shown schematically, the profile of the cured part is believed to follow the top-hatted paraboloid shape as predicated by the photopolymerization theory (Fig. 1).

Figure 7 shows the comparison between the simulation results, observation using the designed schlieren setup, and the corresponding SEM images for two-pixel, six-pixel, and 40-pixel circular images. Such an experiment is necessary to demonstrate the voxel growth dynamics in the PSL process. The first row has the cured parts as observed using the schlieren system. Despite the deviation in the refractive index, the designed system can capture high-

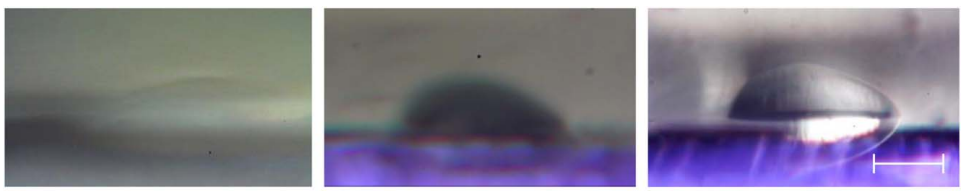

Fig. 5 Voxel observation using (*a*) digital camera alone, (*b*) shadowgraph technique, and (*c*) schlieren optical system. Scale bar size of 80 μm (for (*a*)–(*c*)).

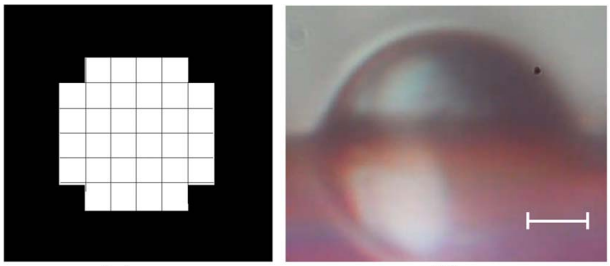

Fig. 6 (*a*) Input binary mask image and (*b*) cured part with a top-hatted paraboloidal profile. Scale bar size of 50 μm.

contrast images. The cured profile is near paraboloid as described by Eq. (6). This is due to the fact that light intensity on the tails of the gaussian light distribution is not strong enough to initiate the photopolymerization. The adjustable confocal optics allows for adaptable magnification settings to accommodate different size of specimen. A digital camera is currently being used in the observation system to record the process of voxel growth at 60 frames per second with a resolution of 640×480. The entire process of the smallest voxel (measuring two pixels) from exposure to termination takes about 7 s, with the first 5 s dedicated to quenching the oxygen-free radicals in the photopolymer resin. The seed generation to termination time takes approximately 2 s. To ensure a precise recording of the growth process, a minimum of 10 frames need to be collected. The second row presents the simulation results as obtained from using equations governing photopolymerization as discussed in Sec. 2. The red portion represents the light energy, whereas the blue portion represents the cured voxel. As can be seen from the images, in the third row, the cured profile matches the simulated profile quite well, which validates our experiments. SEM images in the last row have profiles that match the observed profiles, which validates the robustness of our observation system. The proposed system also has the potential to observe the short-chained polymers. In practical terms, the amount of photopolymerization is reflected in the refractive index of the resin. As the conversion rate increases, the refractive index also increases, but eventually levels off once the photopolymerization is complete. By using a schlieren system to detect even the smallest changes in refractive index, it is possible to define the critical energy for gelation. This has allowed the researchers to critically analyze the gel phase in vat photopolymerization. Minor deviation from the simulation model can be attributed to the simplification of actual interface conditions in the simulation model and the lack of understanding of opto-chemical kinetics at that scale. The thermal effects were not considered during the modeling process, so the shrinkage at the boundary due to temperature change was not considered.

4.4 Validation: Observe Dynamic Polymerization Process.

To validate the effectiveness of the proposed Schlieren system in observing the dynamic photopolymerization process in real-time, experiments were performed to study the rate at which the voxel grows. Images were captured at different time stamps during the photopolymerization process to study the temporal effect. Figure 8 shows voxel growth for a six-pixel pattern projection. As shown in Fig. 9, the physical experimental results agree with the simulation results very well. Temporal data also confirm that the growth rate decreases with penetration depth.

Another set of experiments was done to understand the growth dynamics of a single pixel. Considering the small micromirror size, it is dodgy to study the polymerization for a single pixel due to insufficient energy to cure the resin. Given the light spreading, a 2×2-pixel mask can be considered to follow a similar energy

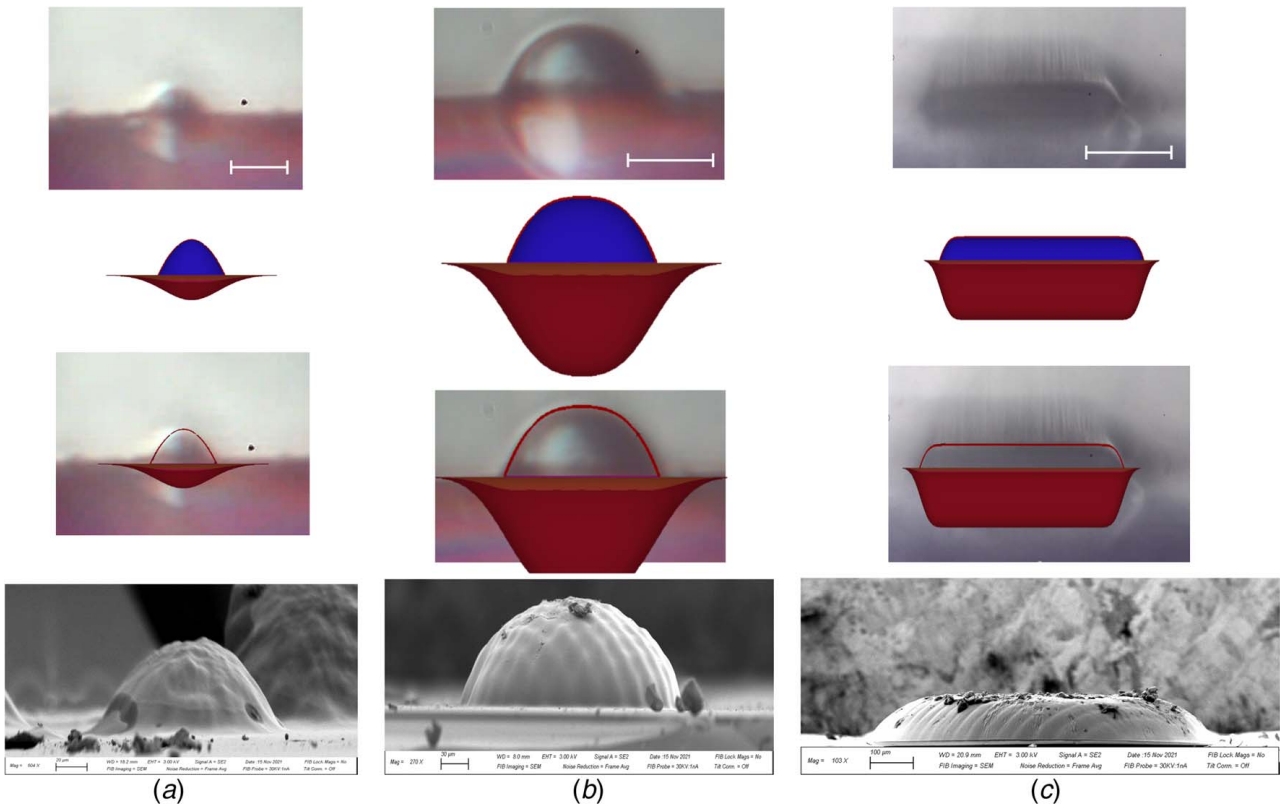

Fig. 7 Comparison between simulated voxel profiles, as observed with schlieren optics, the superimposition of simulation and cured part, and sem images for (*a*) two pixels (scale bar size 30 μm), (*b*) six pixels (scale bar size 50 μm), and (*c*) 40 pixels (scale bar size 150 μm). Energy profile is represented by the bottom profile in red, and the cured profile is represented by the top profile in blue.

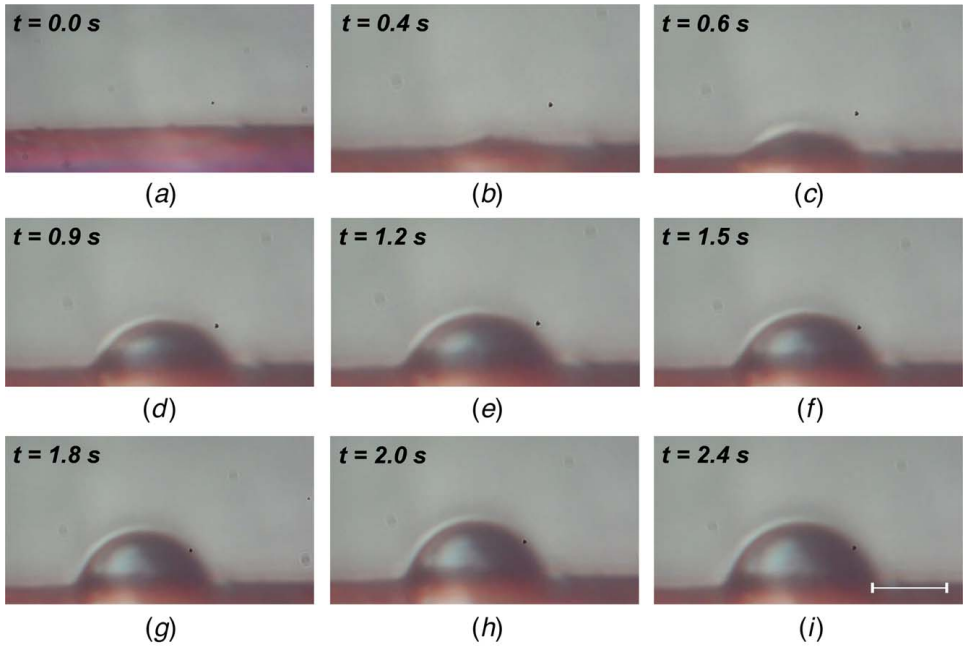

Fig. 8 Voxel shapes at different timestamps during photopolymerization for six-pixel mask (*a*)–(*i*). Scale bar size of 50 μm [27]

profile to a single pixel. Figure 10 shows the voxel growth for a 2 × 2-pixel mask. It is assumed to behave equivalent to a single pixel. The simulated profile in Fig. 11 shows satisfactory correspondence to the actual parts. The designed system allows us to observe the voxel growth in situ, thus eliminating the discrepancies due to cleaning or part removal as seen in Ember's experiments [9].

From the experimental data, the voxel growth rate can be considered uniform in all directions. Thus, the height of the cured part is an appropriate parameter to determine the growth rate. The height of the cured part was measured on the observed image frame using a calibrated digital scale at different timestamps. The height data for the six-pixel image was plotted against the corresponding timestamp as shown in Fig. 12. The same experiment was repeated for a 2 × 2-pixel part as shown in Fig. 13. A logarithmic curve is the best-fitting line through these points, which complies with the theoretical foundation described by Eq. (2). The observed height was compared against the simulations discussed in Sec. 2. Minor discrepancies in the simulated (represented by a red line) and actual growth rate curve (represented by a black line) can be attributed to the fact that our model doesn't account for thermal shrinkage and oxygen inhibition. More specifically, the photopolymerization was delayed during the first 1.0 s due to oxygen inhibition.

4.5 Validation: Robustness and Generality. Dyes are used for altering the resin properties. Dyes absorb photons without creating free radicals and attenuate UV light by scattering light by particles. Despite the scattering, the overall profile of the cured part depends on the light intensity and should follow Gaussian distribution. To validate this, two resin samples with different dye concentrations were prepared. A 40 × 40-pixel image was projected for the same duration on both resins. Dye concentration was found to affect only the penetration depth and not the overall profile of the polymerized part. Cured profile is dependent only on the light intensity and the illumination profile. Changes in the chemical properties of the resin should not affect the spatial profile of the cured part. As seen in Fig. 14, increasing the dye concentration only shortens the height of the cured part maintaining the overall spatial profile.

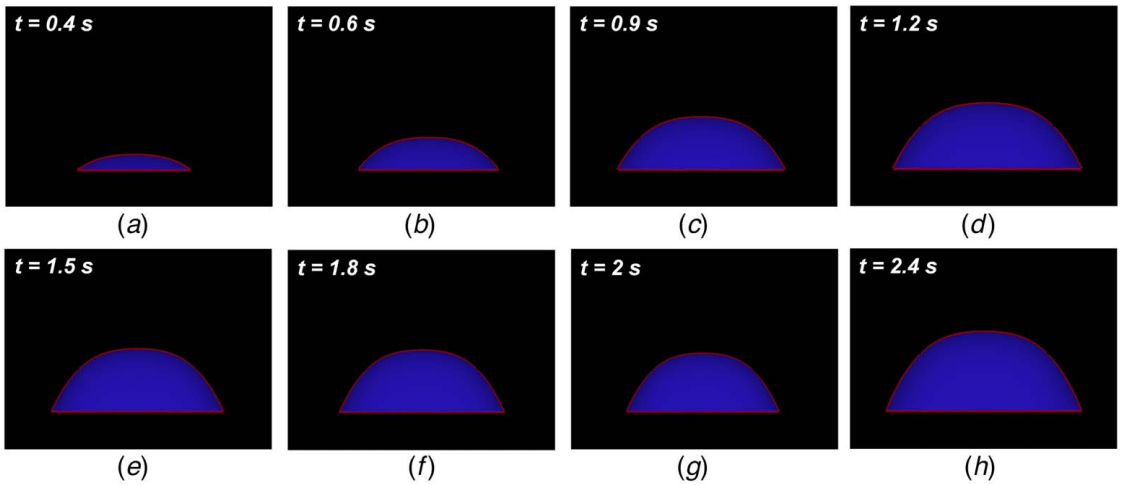

Fig. 9 Simulated voxel growth for six pixels

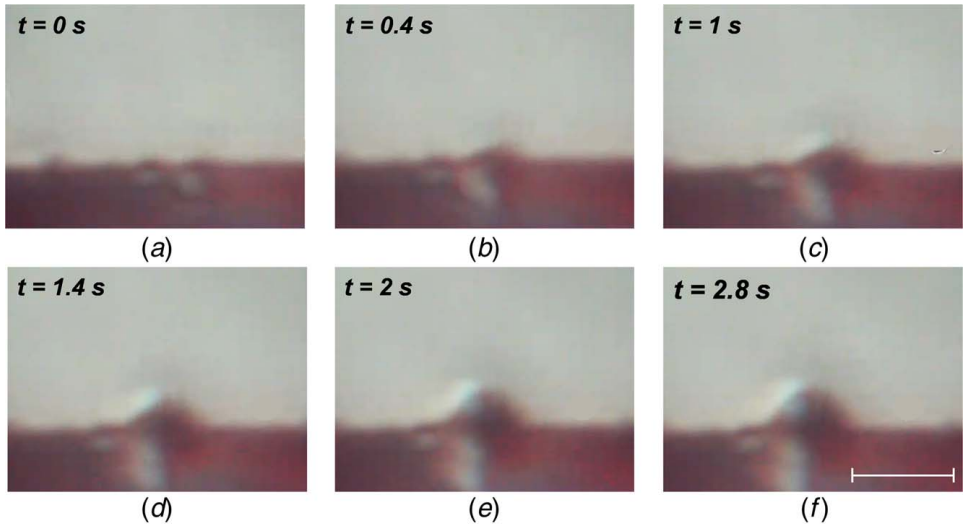

Fig. 10 Voxel shapes at different timestamps during photopolymerization for two-pixel mask (*a*)–(*f*). Scale bar size of 40 μm.

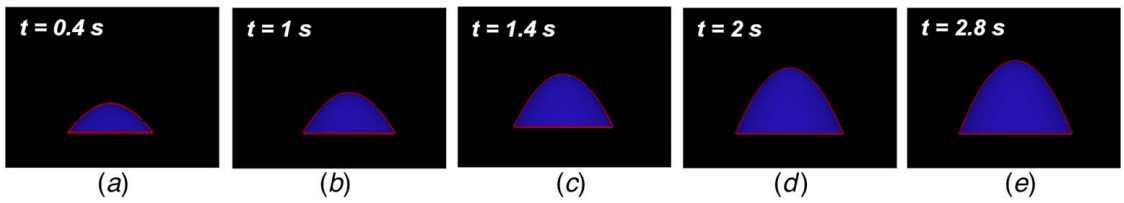

Fig. 11 Simulated voxel growth for two pixels

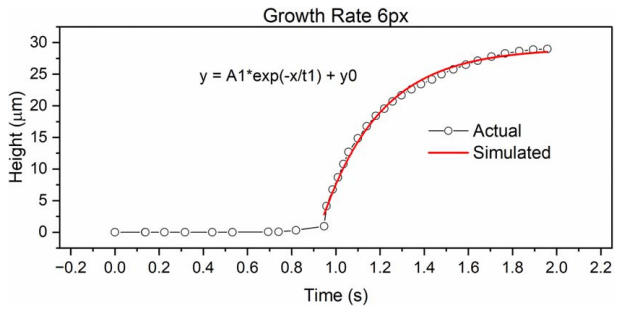

Fig. 12 Photopolymerization rate curve for six pixels: observed (dash and dot) and simulated (solid line)

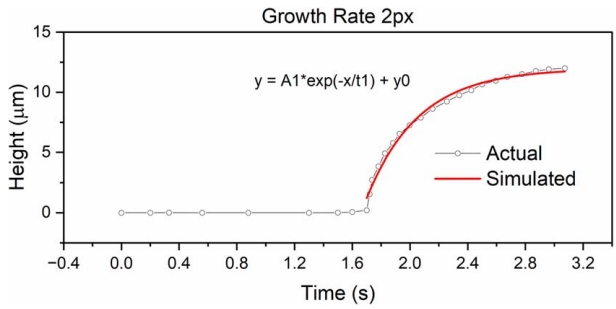

Fig. 13 Photopolymerization rate curve for two pixels: observed (dash and dot) and simulated (solid line)

This verifies the shape function described by Eq. (6), as well as the robustness and generality of the proposed schlieren-based observation system.

Tunable optical setup allowing flexibility in the location of the focal plane was used to match the virtual focal plane with the camera. Accurate positioning of the knife-edge ensured the tenability in the contrast of the image, thus allowing for higher resolution to capture the smaller gradient changes. With the help of confocal magnification, it was possible to observe voxel growth with single-pixel illumination. The optical system can observe micron-scaled voxels, thus addressing the two main challenges that held back the in situ monitoring of the PSL process. By changing the lens configuration, a variable magnification is possible, making this system suitable for observing objects of different sizes. However, the proposed system is limited by material transparency and can only observe polymerization for optically transparent resins. Although, by changing the illumination wavelength, the system has the potential to be used for other optically opaque media as well.

4.6 Application in Microlens Fabrication. Increasing interests in the miniaturization of optoelectronics have attracted significant attention toward the development of micro-optical devices [28,29]. These have found immense applications in imaging, sensing, communication, surface modifications, 3D displays, electronics, and others [30]. Microlenses are small lenses, generally with diameters less than a millimeter and often as low as a few microns. Microlenses have stringent requirements on surface quality, uniformity, and precision. A variety of manufacturing techniques have been developed over the past few decades to cater to these requirements which include thermal reflow, droplet jetting, laser writing, embossing, stereolithography, and micromachining. Despite the relative maturity of these manufacturing processes, limitations like low throughput, long processing times, and challenging quality control still exist [30]. Digital light processing (DLP) technique has high throughput, high resolution, low cost, and superior consistency and is therefore gaining popularity. DLP-based 3D printing creates freeform structures by layer-by-layer localized

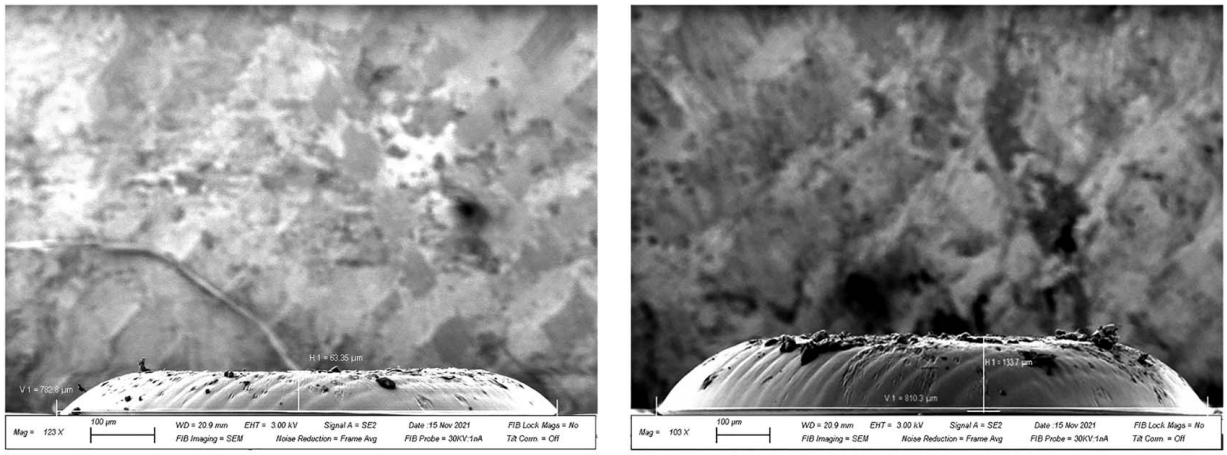

(*a*) (*b*)

Fig. 14 Comparison between two 40-pixel photopolymerized masks for (*a*) 1% w/w, (*b*) 0. 25% w/w dye concentration. Scale bar size of 100 μm.

photopolymerization of UV resin. As this technique uses millions of high-frequency micromirrors grayscale modulation at the pixel level is possible making it an ideal manufacturing process for micro-manufacturing and for creating complex geometries. However, the layer-by-layer approach introduces a micro staircase on the surface. The relative surface roughness fails to satisfy the requirements for micro-optical components [31,32]. The use of a single exposure can reduce surface roughness by eliminating the need for multiple layers and is becoming increasingly popular especially for fabricating sub-100 μm lenses. The single-exposure technique takes advantage of the light energy distribution and grayscaling to achieve the desired curvature. As it is layerless fabrication and void of any moving parts, this approach benefits from high throughput and fidelity. Yuan et.al.'s apporach of realizing optically smooth microlenses by combining UV-single exposure with controlled oscillations successfully eliminated the surface discrepancies caused due to the gaps between the micromirrors [33]. Another smart approach to achieve optical smoothness at the micron level was discussed by Chen et.al. where they used defocussed light to achieve desired shape profile. Light defocussing causes even light spreading resulting in more hemispherical and smoother lenses [34]. Despite the advantages, reliance on the theory-based simulations alone to predict the lens profile results in poor control over the fabrication process and limits on-the-fly modifications to adjust the profile. Theoretical simulations fail to consider all the intricacies of the photopolymerization process which, though inconsequential, may build up giving significant deviations, especially at the tiny scale. Observation-based empirical models can provide a more robust prediction of the curing process. As the schlieren system promotes in situ observation of the curing process, it is possible to implement real-time changes in the input to achieve desired lens profile.

Different applications call for different lens geometries and controlling them with binary exposures alone is implausible. Grayscaling is an approach of controling the energy input by systematic partial illumination of the pixels. Lens contour can be controlled by changing the grayscale gradient. As seen in Fig. 15, different grayscales result in different lens profiles. Binary image results in a flatter top with a box-like profile that matches very well with the simulations as discussed in Sec. 2.3. As the grayscale gradient changes, the profile progresses to a rounder profile. Mask with a gradient grayscale having a central pixel at 255 and edges at 100 results in a hemispherical lens profile as seen in Fig. 15(*d*).

The simulations discussed in Sec. 2.3 and shown in Fig. 15 are based on the assumption that factors like heat, oxygen inhibition, and other chemical kinetics do not contribute to the photopolymerization process. In practice, these factors are very influential in determining the photopolymerization kinetics, especially at the micron scale and at lower energy levels. This leads to reduced contribution from some gray values causing stunted part growth. Oxygen inhibition is a result of oxygen molecules scavenging free radicles, thus increasing the photopolymerization threshold

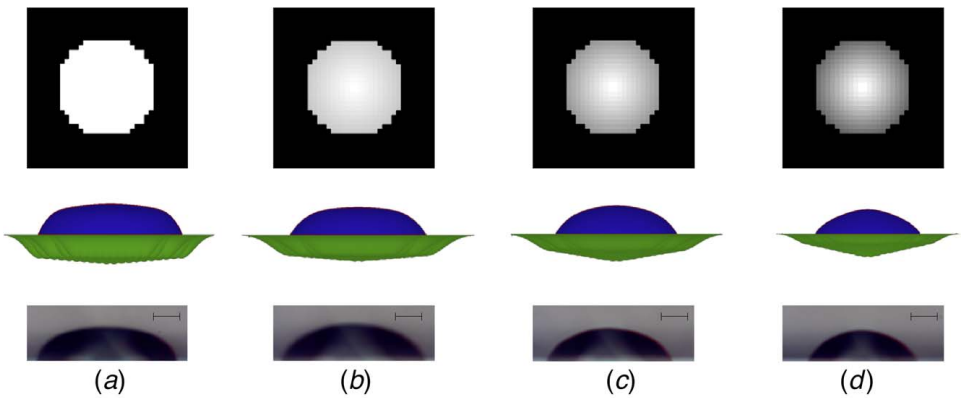

(*a*) (*b*) (*c*) (*d*)

Fig. 15 Grayscale mask, simulated results for the corresponding mask, and observed results with the schlieren system for (*a*) binary mask, (*b*) grayscale ranging from 255 to 200, (*c*) grayscale ranging from 255 to 150, and (*d*) grayscale ranging from 255 to 100. Scale bar size of 100 μm.

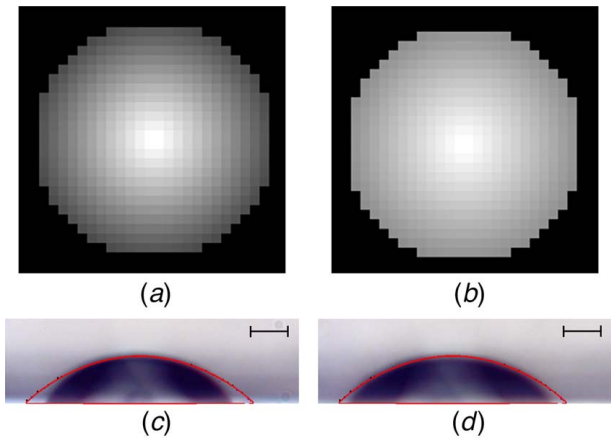

Fig. 16 (*a*) Grayscale 255–70, (*b*) grayscale 255–140, comparison between desired/simulated profile and actual part for (c) gradient grayscale 255–70 (*d*) gradient grayscale 255–140. Scale bar size of 50μm.

and prolonging or at times inhibiting the photopolymerization reaction. Most of the prediction models fail to consider this effect as the amount of dissolved oxygen is difficult to quantify. This leads to some discrepancies in the cured part and the predicted profile, especially at the edges (see Fig. 16(*c*)).

Schlieren-based observations at each step work as a calibration tool to accurately predict the voxel profile. It can be used to map the effect of grayscale and make dynamic changes in the digital mask to compensate for oxygen inhibition. Figure 16 shows the comparison between the cured and simulated profiles. Two grayscale masks with pixel grayscale values 255–70 (Fig. 16(*a*)) and 255–140 (Fig. 16(*b*)) were used to fabricate microlens features. On comparing generated results with simulations, it was observed that the deviations are more significant at lower gray values which need to be compensated in the model for accurate predictions. This can be realized by calibrating the model with the observed data. As the amount of diffused oxygen depends on the chemical properties of the resin, image-based calibration can potentially reduce the prediction error. Although, model calibration and detailed investigation of oxygen inhibition are beyond the scope of this paper. An alternative approach is to introduce a grayscale enhancement to eliminate the deviation between the actual and predicted part.

While a gradient grayscale can give rounder microlenses, most of the lower values barely contribute to the photopolymerization process. Experimental results show a significant deviation from the simulated results at grayscale values below 140. As this deviation cannot be accounted for by the simulations, enhanced grayscale with strategic exposure was used to achieve the desired profile. An energy-grayscale mapping paradigm was introduced to compensate for the deviation with the lowest grayscale restricted at 140. Effective energy similar to the original mask was achieved by controlling the exposure time. As seen in Fig. 16(*d*), the cured part with enhanced mask and controlled exposure matches the desired profile.

Tunability in the exposure energy combined with enhanced grayscale has significantly improved the controlability of microstructures fabricated using single-exposure layerless photopolymerization techniques. An in-depth understsanding of pixel–pixel interactions and oxygen inhibition effect will allow robust prediction models and on-the-fly adjustments in the dynamic masks to realize more complex geometries.

5 Conclusion

In this paper, we investigated voxel growth dynamics during vat photopolymerization using theoretical models and experiments. Different refractive index change-based systems were studied for *in situ* process observation. An optical schlieren system using a single collimated light source was used to capture the variations in refractive index caused by the distortion of the collimated light beam due to density gradients. Experimental results were compared against a simulation model based on Beer–Lambert's law, photopolymerization growth curve, and theories of *Gaussian* beam propagation. The use of confocal lenses provides high magnification of the test region while keeping the overall setup limited to a small size. The voxel growth dynamics have been investigated based on the refractive index gradient corresponding to the degree of monomer conversion. The experimental results are compared against the simulation model based on the theoretical understanding of Beer's law and photopolymerization kinetics. However, important factors like oxygen inhibition and thermal effects were ignored. The current system is capable of characterizing voxel growth in optically transparent materials. Further investigation is necessary to modify this system for opaque resins. The effect of oxygen inhibition was witnessed while fabricating microlenses using grayscale but its investigation is beyond the scope of this work. A novel energy-grayscale mapping paradigm was briefly introduced to compensate for the size deviation occurring due to oxygen inhibition and its potential was examined for microlens fabrication. Microlenses fabricated with enhanced grayscale provided a better matching lens profile to the predicted results. Further investigation on the grayscale-energy mapping strategy is needed to achieve robust fabrication. The implementation of a similar system for characterizing thermal effects during photopolymerization should be investigated.

Acknowledgment

The authors would like to gratefully acknowledge the support from the National Science Foundation (NSF) (Grant Nos. CMMI-1846863 and ECCS-2111056).

Conflict of Interest

There are no conflicts of interest.

Data Availability Statement

The data sets generated and supporting the findings of this article are obtainable from the corresponding author upon reasonable request.

References

[1] Gibson, I., Rosen, D. W., Stucker, B., and Khorasani, M., 2021, *Additive Manufacturing Technologies*, Springer, New York.
[2] Hu, Y., Guo, Z., Ragonese, A., Zhu, T., Khuje, S., Li, C., Grossman, J. C., Zhou, C., Nouh, M., and Ren, S., 2020, "A 3D-Printed Molecular Ferroelectric Metamaterial," Proc. Natl. Acad. Sci. U. S. A., **117**(44), pp. 27204–27210.
[3] Anandakrishnan, N., Ye, H., Guo, Z., Chen, Z., Mentkowski, K. I., Lang, J. K., Rajabian, N., Andreadis, S. T., Ma, Z., and Spernyak, J., 2021, "Fast Stereolithography Printing of Large-Scale Biocompatible Hydrogel Models," Adv. Healthcare Mater., **10**(10), p. 2002103.
[4] Lin, D., Jin, S., Zhang, F., Wang, C., Wang, Y., Zhou, C., and Cheng, G., 2015, "3D Stereolithography Printing of Graphene Oxide Reinforced Complex Architectures," Nanotechnology, **26**(43), p. 434003.
[5] Zhou, C., Chen, Y., and Waltz, R., 2009, "Optimized Mask Image Projection for Solid Freeform Fabrication," ASME J. Manuf. Sci. Eng., **131**(6), p. 061004.
[6] Cerwonka, E., and Millard, F. W., 1963, *Investigation of the Photopolymerization Process*, General Aniline and Film Corporation, Johnson City, NY.
[7] Dong, M. K., Goyal, K. G., Worth, B., Makkar, S., Calhoun, W. R., Bali, L. M., and Bali, S., 2013, "Accurate in Situ Measurement of Complex Refractive Index and Particle Size in Intralipid Emulsions," J. Biomed. Opt., **18**(8), p. 087003.
[8] Emami, M. M., and Rosen, D. W., 2018, "An Improved vat Photopolymerization Cure Model Demonstrates Photobleaching Effects," Proceedings of the Solid Freeform Fabrication Symposium, Austin, TX, Aug. 13–15, pp. 1940–1952.
[9] Ember Printer, 2016, How a Voxel Grows, https://www.instructables.com/Ember-Printer-How-a-Voxel-Grows/.
[10] Fernandez Fernandez, A., Brichard, B., and Berghmans, F., 2003, "In Situ Measurement of Refractive Index Changes Induced by Gamma

Radiation in Germanosilicate Fibers," IEEE Photonics Technol. Lett., **15**(10), pp. 1428–1430.
[11] Vaglieco, B. M., Beretta, F., and d'Alessio, A., 1990, "In Situ Evaluation of the Soot Refractive Index in the UV-Visible From the Measurement of the Scattering and Extinction Coefficients in Rich Flames," Combust. Flame, **79**(3–4), pp. 259–271.
[12] Li, X., and Chen, Y., 2017, "Micro-Scale Feature Fabrication Using Immersed Surface Accumulation," J. Manuf. Process., **28**, pp. 531–540.
[13] Emami, M. M., and Rosen, D. W., 2020, "Modeling of Light Field Effect in Deep Vat Polymerization for Grayscale Lithography Application," Addit. Manuf., **36**, p. 101595.
[14] Settles, G. S., and Covert, E. E., 2002, "Schlieren and Shadowgraph Techniques: Visualizing Phenomena in Transport Media," ASME Appl. Mech. Rev., **55**(4), pp. B76–B77.
[15] Zhou, C., Ye, H., and Zhang, F., 2014, "A Novel Low-Cost Stereolithography Process Based on Vector Scanning and Mask Projection for High-Accuracy, High-Speed, High-Throughput and Large-Area Fabrication," Proceedings of the International Design Engineering Technical Conferences and Computers and Information in Engineering Conference, Buffalo, NY, Aug. 17–20, Vol. 46285, American Society of Mechanical Engineers, p. V01AT02A068.
[16] Zhou, C., and Chen, Y., 2009, "Calibrating Large-Area Mask Projection Stereolithography for Its Accuracy and Resolution Improvements," Proceedings of Solid Freeform Fabrication Symposium, Austin, TX, Aug. 3–5.
[17] Zhou, C., Xu, H., and Chen, Y., 2021, "Spatiotemporal Projection-Based Additive Manufacturing: A Data-Driven Image Planning Method for Subpixel Shifting in a Split Second," Adv. Intell. Syst., **3**(12) p. 2100079.
[18] Zhou, C., and Chen, Y., 2012, "Additive Manufacturing Based on Optimized Mask Video Projection for Improved Accuracy and Resolution," J. Manuf. Process., **14**(2), pp. 107–118.
[19] Jacobs, P. F., 1992, *Rapid Prototyping & Manufacturing: Fundamentals of Stereolithography*, Society of Manufacturing Engineers, Dearborn, MI.
[20] Hwang, J. W., Noh, S. M., Kim, B., and Jung, H. W., 2015, "Gelation and Crosslinking Characteristics of Photopolymerized Poly (Ethylene Glycol) Hydrogels," J. Appl. Polym. Sci., **132**(22).
[21] Toepler, A., 1993, *SPIE Milestone Series MS*, Vol. 61, SPIE Press.
[22] Krehl, P., and Engemann, S., 1995, "August Toepler—the First Who Visualized Shock Waves," Shock Waves, **5**(1), pp. 1–18.
[23] Huang, C., Gregory, J. W., and Sullivan, J. P., 2007, "A Modified Schlieren Technique for Micro Flow Visualization," Meas. Sci. Technol., **18**(5), p. N32–N34.
[24] Mazumdar, A., 2013, *Principles and Techniques of Schlieren Imaging Systems*, Department of Computer Science, Columbia University, New York.
[25] Agarwal, S., Mallick, S. P., Kriegman, D., and Belongie, S., 2004, "On Refractive Optical Flow," European Conference on Computer Vision, Prague, Czech Republic, May 11–14, Springer, pp. 483–494.
[26] Tropea, C., Yarin, A. L., and Foss, J. F., 2007, *Springer Handbook of Experimental Fluid Mechanics*, Springer, New York.
[27] Chivate, A., 2022, Voxel Growth Observation Using Schlieren, https://chizhouub.github.io/public/JMSE/Voxel_growth_video.mp4.
[28] Camposeo, A., Persano, L., Farsari, M., and Pisignano, D., 2019, "Additive Manufacturing: Applications and Directions in Photonics and Optoelectronics," Adv. Opt. Mater., **7**(1), p. 1800419.
[29] Hou, T., Zheng, C., Bai, S., Ma, Q., Bridges, D., Hu, A., and Duley, W. W., 2015, "Fabrication, Characterization, and Applications of Microlenses," Appl. Opt., **54**(24), pp. 7366–7376.
[30] Yuan, W., Li, L.-H., Lee, W.-B., and Chan, C.-Y., 2018, "Fabrication of Microlens Array and Its Application: A Review," Chin. J. Mech. Eng., **31**(1), pp. 1–9.
[31] Sun, C., Fang, N., Wu, D. M., and Zhang, X., 2005, "Projection Micro-Stereolithography Using Digital Micro-Mirror Dynamic Mask," Sens. Actuators, A, **121**(1), pp. 113–120.
[32] Gao, Y., He, S., Luo, N., and Rao, Y., 2011, "Research on Dynamical-Gradual Greyscale Digital Mask Lithography," J. Mod. Opt., **58**(7), pp. 573–579.
[33] Yuan, C., Kowsari, K., Panjwani, S., Chen, Z., Wang, D., Zhang, B., and Ng, C. J.-X., 2019, "Pablo Valdivia Y Alvarado, and Qi Ge, Ultrafast Three-Dimensional Printing of Optically Smooth Microlens Arrays by Oscillation-Assisted Digital Light Processing," ACS Appl. Mater. Interfaces, **11**(43), pp. 40662–40668.
[34] Chen, P.-C., Yeh, C.-S., and Hsieh, C.-Y., 2022, "Defocus Digital Light Processing Stereolithography for Rapid Manufacture of Microlens Arrays," Sens. Actuators, A, **345**, p. 113819.
[35] Panigrahi, P. K., and Muralidhar, K., 2012, "Laser Schlieren and Shadowgraph," *Schlieren and Shadowgraph Methods in Heat and Mass Transfer*, Springer, New York, pp. 23–46.